Nano Energy 119 (2024) 109057

Contents lists available at ScienceDirect

Nano Energy

journal homepage: www.elsevier.com/locate/nanoen

Flag-type hybrid nanogenerator utilizing flapping wakes for consistent high performance over an ultra-broad wind speed range

Liwei Dong [a,b], Qian Tang [c], Chaoyang Zhao [b], Guobiao Hu [d], Shuai Qu [b,e], Zicheng Liu [b], Yaowen Yang [b,*]

[a] Institute of Rail Transit, Tongji University, Shanghai 201804, China
[b] School of Civil and Environmental Engineering, Nanyang Technological University, 50 Nanyang Avenue, Singapore 639798, Singapore
[c] Chongqing Key Laboratory of Green Energy Materials Technology and System, Chongqing University of Technology, Chongqing 400054, China
[d] Internet of Things Thrust, The Hong Kong University of Science and Technology (Guangzhou), Nansha, Guangzhou, Guangdong 511400, China
[e] Train and Track Research Institute, State Key Laboratory of Traction Power, Southwest Jiaotong University, Chengdu 610031, China

ARTICLE INFO

Keywords:
Wind energy harvesting
Flag-type
Hybrid nanogenerator
Wake effect
Wireless sensor node

ABSTRACT

Fluttering of regular flags and flapping of inverted flags in the wind serve as the foundational principles of flag-type nanogenerators (FNGs). However, FNGs relying on a single aerodynamic behavior exhibit significant power output only within a limited spectrum of wind speeds, posing a challenge to their robustness in scenarios with intensely fluctuating wind. In this paper, we propose a novel hybrid scheme aimed at harnessing the synergistic potential of two aerodynamic behaviors to enhance the performance of FNGs and broaden their operational wind speed ranges. A flag-type triboelectric-piezoelectric hybrid nanogenerator (FTPNG) is developed with the integration of flapping piezoelectric flags (PEFs) and a fluttering triboelectric flag (TEF). To overcome the limited operational wind speed range, flapping PEFs are configured in an array format, optimized through fluid-solid coupled simulations. The rear TEF leverages the fluttering motion of a polytetrafluoroethylene (PTFE) membrane, which intermittently contacts and separates from conductive textiles positioned on the inner surface of the baffles. A noteworthy feature is the innovative "back-to-back" design, which utilizes the flapping wakes generated by PEFs to intensify the fluttering of the PTFE membrane, resulting in a remarkable boost in power generation of up to 132 times and achieving a maximum peak power output of 5400 μW. The FTPNG offers consistent high performance, with an average output of exceeding 200 μW over an ultra-broad wind speed range of 4.7–14.6 m/s, while the complete operational range is 3.7–15 m/s. It also attains a considerable average power output of 850 μW at 7.8 m/s, marking a significant advancement compared to other FNGs. Finally, in demonstration tests, the FTPNG can light 252 LEDs and showcases the capabilities of PEF array and TEF to independently power a wireless sensor node (WSN), highlighting its significant potential for applications in the Internet of Things and various self-powered systems.

1. Introduction

The advent of artificial intelligence and big data era has significantly underscored the importance of deploying and acquiring data from wireless sensor nodes (WSNs). The latest generation of wireless sensor nodes is characterized by a strong drive toward miniaturization, portability, and low power consumption [1]. Simultaneously, the emergence of energy harvesting technologies leveraging ambient renewable energy sources offers an eco-friendly alternative to traditional batteries, helping to lessen chemical pollution and reduce the need for follow-up maintenance [2]. Wind energy, being both ubiquitous and widely distributed, can be harnessed to make the power supply more flexible and convenient [3]. Therefore, nanogenerators designed for harvesting wind energy have garnered considerable attention in pursuing highly integrated and self-sufficient WSNs.

Small-scale and micro-scale wind energy harvesters typically employ mechanisms including piezoelectric [4,5], electromagnetic [6,7], triboelectric [8,9], and their hybrid configurations [10–13]. Among these, flag-type nanogenerators (FNGs), inspired by the flag fluttering in the wind, have attracted the interest of researchers due to their innate

* Corresponding author.
E-mail address: cywyang@ntu.edu.sg (Y. Yang).

https://doi.org/10.1016/j.nanoen.2023.109057
Received 25 September 2023; Received in revised form 14 October 2023; Accepted 31 October 2023
Available online 4 November 2023

flexibility, pliability, and potential for miniaturization. Flag-type piezoelectric nanogenerators (PENGs) are usually fabricated with piezoelectric materials such as polyvinylidene fluoride (PVDF) films [14,15] and ZnO nanowires [16]. Since Wang et al. [17] first proposed the concept of triboelectric nanogenerator (TENG) in 2012, we have witnessed the persistent development of TENGs over the past years [18–21]. TENGs have exhibited impressive potential in self-powered sensing [22,23], battery-free Internet of Things (IoTs) [24], blue energy [25], and wearable electronics [26]. The advancement of TENG technology has opened the door for designing more versatile FNGs. Most of them are designed based on contact-separation mode or free-standing mode. By interweaving or adhering two triboelectric materials with opposite electron affinities [27–29], the twisting and bending motions during flag fluttering engender the contact-separation mode. Additionally, configuring baffles on one or both sides of the flag [30,31] or utilizing the fluttering contact between the two flags have also yielded different flag-type TENGs [32]. Hybrid energy harvesting with enhanced electrical output has emerged as a solution to overcome the inherent limitations of using a single power generation mechanism [33]. The triboelectric-electromagnetic hybridization is favored for wind energy harvesting [34–36] since TENGs with high-voltage output and electromagnetic generators (EMGs) with high-current output can complement each other [37]. Moreover, combining the distinct advantages of TENGs at low frequencies and EMGs at high frequencies [38] helps facilitate the effective expansion of the operational bandwidth [38]. The impressive power density, flexibility, and miniaturization potential of PENGs enable them to be strong candidates for integration with TENGs in highly integrated designs [39,40]. The wind energy harvesting performance of TENGs can also be enhanced with the hybridization of multiple working modes. Zou et al. [41] proposed a self-regulation strategy for the TENG utilizing nonlinear magnetic forces to switch the working mode, thus achieving better robustness and performance across a broad operational wind speed range. For the hybridization of FNGs, Ye et al. [42] integrated a flag-type TENG with a rotary TENG and an EMG, which resulted in a wider operational wind speed range and improved overall performance. Jorge et al. [43] incorporated solar cells at the ends of piezoelectric flags (PEFs) to enable simultaneous wind and solar energy harvesting. Though this integration slightly affected the output of PEFs, the overall output power was significantly improved. Wind direction is another key factor affecting the performance of FNGs. Unlike rotary wind energy harvesting systems, FNGs typically face challenges in sustaining high performance when confronted with substantial variations in wind direction. Consequently, external mechanisms or mechanical modulations [44,45] become imperative for assisting them in aligning with the wind direction. The most frequently employed and reliable scheme is to combine them with wind vanes, ensuring their robustness and overall performance in natural environments [46,47].

Regardless of energy conversion mechanisms, FNGs can be divided into two categories from the dynamics perspective. Regular flags flutter when the wind flows across their clamped edge, and the harvesters that utilize the mechanical energy of flag flutter are known as “flutter-driven nanogenerators” [27–32,48,49]. Their dominant vibration modes are intricately linked to the bending stiffness and mass ratio, which needs careful design to trigger the energetic fluttering regime for efficient wind energy harvesting [50–52]. More importantly, by configuring upstream bluff bodies and utilizing the downstream wakes, the cut-in wind speed of flutter-driven nanogenerators can be lowered, and their performance can be enhanced [53–55]. Other research demonstrated that the metasurface design on the bluff body can further boost wind energy harvesting efficiency [56–58]. Latif et al. [59,60] systematically investigated the effects of different bluff bodies on flag aerodynamics. They found that the 120-degree bluff body can maximize the performance due to its induced strong wake region. They also utilized the wakes generated by two cylinders to boost the performance of flutter-driven nanogenerators, and analyzed the influences of cross-stream and lateral gaps on flapping dynamics [61]. In addition, Zhang et al. [62] employed a flexible flagpole to improve the fluttering mechanical energy of the flutter-driven TENGs, and boosted the output power by up to 113 times.

Conversely, when wind flows across the leading edge of flags and results in reciprocating flapping motion, they are called “inverted flags”. Wind energy harvesters based on inverted flags can be classified as “flap-driven nanogenerators” [43,46,63]. Inverted flags are theoretically capable of generating more than ten times strain energy than conventional flags [64]. Numerous two-dimensional simulations revealed that the dynamic response of inverted flags is bound up with parameters including the bending stiffness, inertia and Reynolds number, and their motion states can be divided into straight, flapping, and deflected modes [65,66]. To break through the limitations of simulations, Orrego et al. [46] experimentally proved that a larger width-length ratio is beneficial for widening operational bandwidth and demonstrated the ability of a flap-driven nanogenerator to continuously power sensors.

The operational wind speed range and performance of FNGs are profoundly influenced by their material properties, composite structures and geometric parameters. The prerequisite for achieving high performance is to customize these factors reasonably according to environmental wind speeds. Nonetheless, the dominant power outputs of most FNGs remain confined to a narrow operational bandwidth, leading to poor robustness in various scenarios with fluctuating wind speeds. Severe challenges have been posed in developing FNGs towards efficiency and broadband:

- Flutter-driven nanogenerators, while offering a broad operational bandwidth, often come with relatively high cut-in wind speeds [62], and their fluttering response and power output increase sharply with wind speed, leading to inadequate power generation at low and middle wind speeds.
- Flap-driven nanogenerators, although capable of delivering a consistently notable power output, contend with a narrow operational bandwidth [65,66]. This limitation hinders their compatibility with a wide variety of wind speeds.
- The high-integration and high-performance hybridization schemes for FNGs face great challenges. Flag responses are easily affected by structure or wind field variations, resulting in performance degradation. Hence, it is crucial to focus on the design of FNGs to prevent any potentially harmful mutual interference between these nanogenerators.

To address the above issues raised, we develop a solution that harmoniously harnesses the benefits of flap-driven and flutter-driven nanogenerators, and propose a hybridization scheme capable of considerable power output over an ultra-broad range of wind speeds. The flag-type triboelectric-piezoelectric hybrid nanogenerator (FTPNG) is composed of a piezoelectric flag array (PEFA) in the flapping mode and a triboelectric flag (TEF) in the fluttering mode with a back-to-back layout. To broaden the limited bandwidth of a single PEF, three PEFs form the PEFA encompassing an operational range from 3.7 to 14.6 m/s. The geometric parameters are carefully determined based on fluid-solid coupled simulation. In addition, PEFA acts as a “performance booster” and enhances the output of TEF up to 132 times due to more intense TEF fluttering induced by its flapping wakes. The effects of the aspect ratio and the longitudinal and lateral distances D_1 and D_2 on the performance of TEF are investigated. Experimental results showcase the FTPNG achieves a maximum average power of 850 μW at 7.8 m/s, and can guarantee an average power greater than 200 μW over wind speeds ranging from 4.7 to 14.6 m/s. Overall, the proposed FTPNG offers an effective and low-cost power supply solution for WSNs towards a broad spectrum of wind conditions.

2. Results and discussion

2.1. Configuration and working principle of the FTPNG

Thanks to the diverse working modes of TENGs and the flexibility of PENGs, the FTPNG first integrates flutter-driven and flap-driven nanogenerators to achieve a consistent high performance over an ultra-broad wind speed range. It is proposed as a sustainable power source to implement self-powered applications in places with abundant wind sources. Fig. 1a illustrates a potential application scenario of FTPNG for powering nearby electronics at the trackside. To guarantee adaptability for wind direction variations and high performance in natural environments, the FTPNG and a wind vane can be combined and fixed on the same spindle for synchronized direction adjustment, as shown in Fig. S1. Actually, many application scenarios, such as car roofs and roadsides in rail and road transportation, as well as highland areas and seaside areas, need a broader operational bandwidth to adapt to significant changes in wind speed. This is also the motivation of this study to develop the FTPNG for broadband wind energy harvesting. The overall structure of FTPNG is illustrated in Fig. 1b. The PEFA and the TEF are ingeniously integrated in a "back-to-back" configuration to enable a more compact structure. They are interlinked by the flagpole with a cable housing box. The front part of two baffles on both sides of TEF is hollowed out to ensure the normal flow of wind. When the wind flows across the PEFA, the reasonably designed PEFA will generate a self-sustained flapping. The reciprocating flapping induces periodic wakes flowing to the nearby area of TEF, thereby stimulating its fluttering, as shown in Fig. 1c. The TEF fluttering induced by flapping wakes is proven to be more intense than that in the case when the wind directly flows across it. Consequently, the FTPNG is not only a hybridization of triboelectric and piezoelectric mechanisms, but also a conception leveraging the aerodynamic behavior of flap-driven nanogenerators to boost the performance of flutter-driven nanogenerators. The improvement that comes with it will be quantified in Section 2.4. To demonstrate the superiority of this approach, the TEF in the FTPNG is compared to other TNGs in Fig. 1d. The TEF with the PEFA enhancement achieves an average power of 820 μW at 7.8 m/s as well as an operational range of 3.7–15 m/s, which are both superior in triboelectric and piezoelectric FNGs. Even at a relatively low wind speed of 4.7 m/s, the power output of 208 μW also surpasses most FNGs. Notably, the performance is consistent over 200 μW across the operational range of 4.7–14.6 m/s, thus we designate this range as a high-performance region. This indicates a considerable output of TEF in an ultra-broad bandwidth even without considering the power generation of PEFA.

A detailed configuration of PEFA is illustrated in Fig. 2a. Given the limited bandwidth of a single PEF, three PEFs are incorporated in the PEFA to harvest wind energy at low, middle, and high speeds, respectively. PEFs for low and middle wind speeds are implemented with adjustments in their geometric parameters, and each PEF is composed of two PVDF films physically connected in parallel. General PEFs exhibit insufficient bending stiffness to trigger the self-sustained flapping at high wind speeds. Therefore, a stainless steel film is employed in the PEF for high-speed wind as the substrate to enhance the bending stiffness and provide the restoring force. A total of four PVDF films are attached on both sides of the stainless steel film. The evolution of the flag flapping is illustrated in Fig. 2b. The PEF is a flap-driven nanogenerator with a free leading edge and a clamped trailing edge. When the wind goes through it, a small oscillation is triggered in the free leading edge and gradually evolves into approximately periodic flapping due to the instability of fluid and solid. Remarkably, the deflection angle of self-sustained flapping can be substantial (over 90°) [64], thus generating large strain energy. When the free leading edge of PEFs bends upwards, the upper surface of PVDF films suffers from mechanical stress while the lower surface undergoes mechanical strain. Consequently, negative and positive charges are generated on the upper and lower surfaces, respectively, due to the piezoelectric effect, resulting in a transient current in the

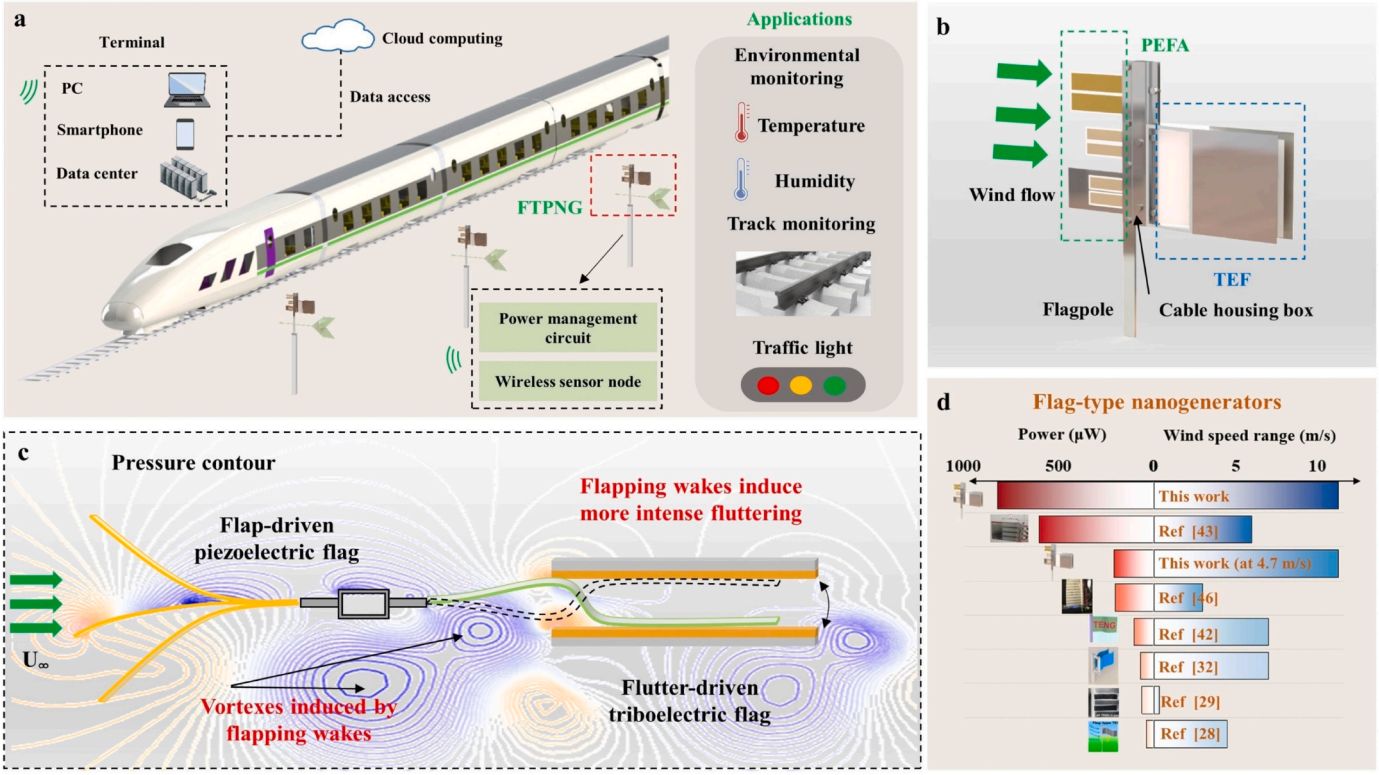

Fig. 1. Structure of FTPNG and its applications: (a) potential applications of FTPNG; (b) structural configuration of FTPNG; (c) schematic of the performance of FET enhanced by flapping wakes of PETA; (d) comparison of the power performance and oerational bandwidth with FNGs (only the TEF part of FTPNG is used for comparison).

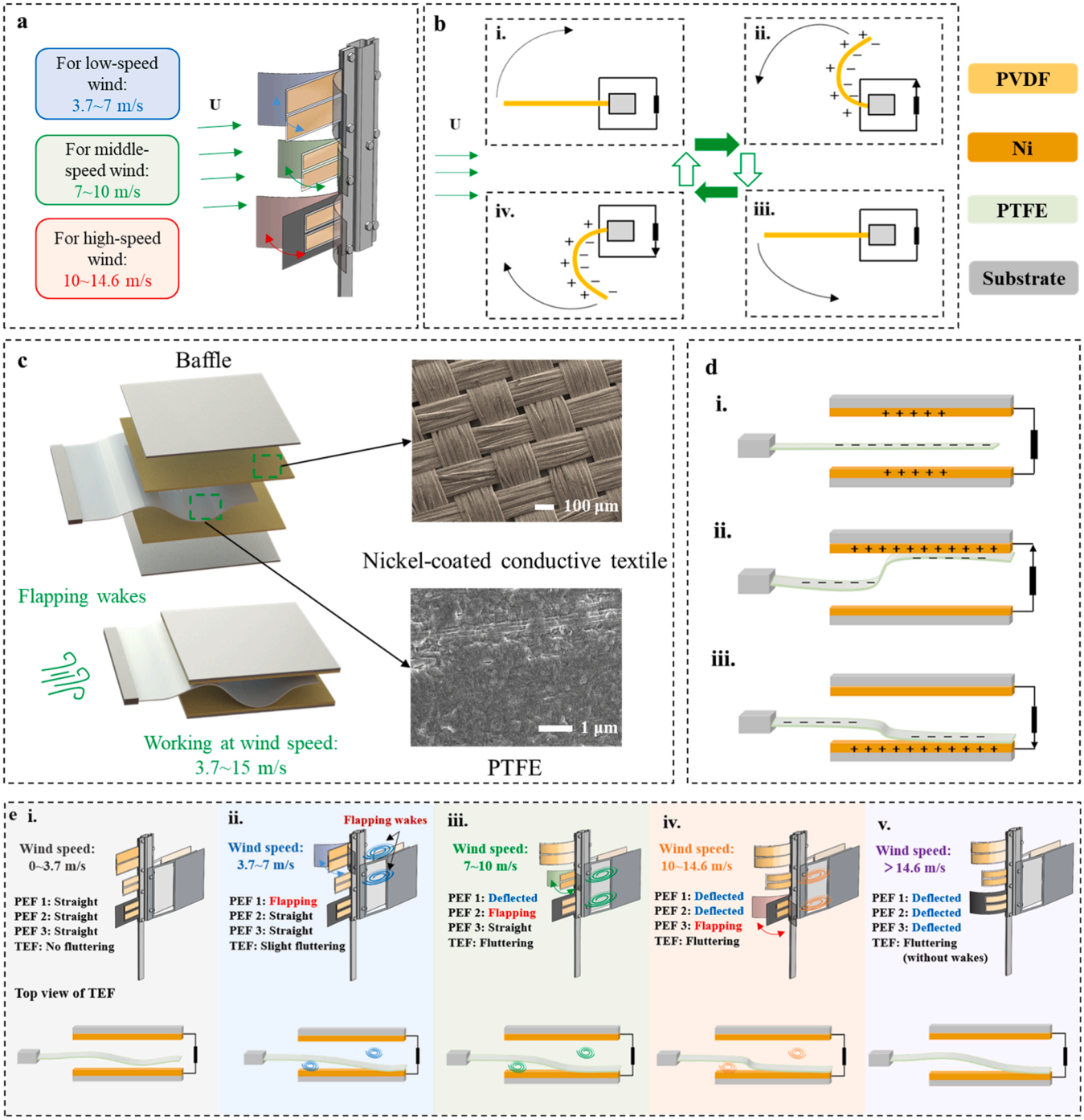

Fig. 2. Working principle and materials of FTPNG: (a) configuration of PEFA and its sub flags; (b) schematic of the working principle of PEFs; (c) scheme of TEF and its materials; (d) working mechanism of the free-standing mode of TEF; (e) five working states of FTPNG (two PEFs may flap simultaneously during the working state transition, and the work status is divided based on the current main flapping PEF).

external circuit (see Fig. 2b-i to b-iii). When the bending direction is downward, the charge polarity on the two surfaces and the current direction are reversed (see Fig. 2b-iii to b-i). Typical voltage curves of PEFA are depicted in Fig. S2.

Fig. 2c illustrates the scheme of TEF and its materials. The trigger condition of TEF fluttering is contrary to PEFs, where the leading edge is clamped, and the trailing edge is free. Due to the cable housing box behind the flagpole, the clamped leading edge should maintain a certain distance from baffles in the longitudinal direction to ensure that the wind flows into the inner side of baffles, which is structurally different from common flutter-driven nanogenerators [30,31]. The main body of the flag is a polytetrafluoroethylene (PTFE) membrane. The Ni-coated conducive textiles are attached on the inner side of two baffles, creating opportunities for contact and separation during the fluttering of the PTFE membrane. The images of two materials under the scanning electron microscope (SEM) are depicted in Fig. 2c. The free-standing working mode of TEF is demonstrated in Fig. 2d. In the initial state, the PTFE membrane remains separated from the conductive textiles on both sides. Charges with opposite polarity are generated on two materials under the electrostatic induction effect (see Fig. 2d-i). Subsequently, as the wind excites the fluttering of the PTFE membrane, it comes into contact with the upper conductive textile. The positive

charges transfer to the upper conductive textile, generating a transient current in the circuit (see Fig. 2d-ii). Conversely, all the positive will transfer to the lower conductive textile when the PTFE membrane flaps onto it. Meanwhile, a transient current with an opposite flow direction occurs in the circuit (see Fig. 2d-iii). The typical voltage and transfer charge of TEF are illustrated in Fig. S3.

Fig. 2e illustrates five working states of FTPNG. When the wind speed U ≤ 3.7 m/s, all the PEFs are in the straight mode, and the TEM hardly flutter (see Fig. 2e-i). The flapping mode of PEF 1 is triggered over 3.7 ≤U< 7 m/s. A portion of its generated wakes diffuses vertically and induces a slight TEF fluttering (see Fig. 2e-ii). When PEF 2 (7 ≤U<10 m/s) or PEF 3 (10 ≤U<14.6 m/s) comes into the flapping mode, their flapping wakes flow towards the rear TEF and induce an intense fluttering (see Fig. 2e-iii and iv). When U> 14.6 m/s, the three PEFs are all deflected and obstruct the airflow; thereby, the degree of the TEF fluttering will be weakened (see Fig. 2e-v).

2.2. Broadband design and performance of the PEFA

For thin flags/plates in uniform flow, the non-dimensional bending stiffness K_b is validated as a key parameter that determines the critical wind speed in numerous two-dimensional simulation studies [65,66]. When K_b> 0.3, 0.1 ≤K_b≤ 0.3 and K_b< 0.1, flags in wind flow work in straight, self-sustained flapping and deflected modes, respectively. The self-sustained flapping mode is the main status for energy harvesting, where the peak-to-peak deformation amplitude (the ratio of the oscillation amplitude to the flag length) can be up to 1.7–1.8 [64]. The mass ratio M^* is another non-dimensional parameter related to the flapping frequency and the bending curvature [46].

$$K_b = \frac{EH^3}{12(1-v^2)\rho_f U^2 L^3} \tag{1}$$

$$M^* = \frac{\rho_s H}{\rho_f L} \tag{2}$$

where E represents Young's modulus of the flag material; H represents the flag thickness; v refers to the Poisson's ratio; ρ_f and ρ_s are the fluid and solid densities; U represents the wind speed; and L is the flag length.

To ensure comprehensive coverage of broad wind speed range and seamless transitions between the working regions of PEFs, the COMSOL Multiphysics software is employed to facilitate the fluid-solid coupled simulations to optimize geometric parameters. The computational layout is supplied in Fig. S4. The determined geometric dimensions are illustrated in Fig. 3a. Fig. 3b shows the screenshots of the instantaneous velocity field of the three PEFs at 6, 10, and 14 m/s, respectively. The evolution of the flapping-induced velocity field in a half period is illustrated in Fig S5. During the flapping status, the maximum velocity is observed in the leading edge, while the rear end of PEFs is filled with periodic wakes. Fig. 3c presents a general rule: within the working wind speed range, the peak-to-peak flapping angle exhibits a positive correlation with the wind speed, while the flapping frequency negatively correlates with it. Based on the simulation design, three PEFs are tailored to cover the specific wind speed intervals, namely 3.5–7.5, 6–13, and 8.5–15.5 m/s, respectively. Subsequently, a series of tests are conducted to validate the flag simulation. The experimental setup is illustrated in Fig. S6, and the test results are compared with the simulation results in Fig. S7. From the flapping angle and frequency perspectives, the simulation data closely aligns with the test results. Due to potential variations in fluid uniformity and initial flag angle that cannot be perfectly controlled during tests, the self-sustained flapping may be dampened in advance with the wind speed approaching the critical value. As a result, the actual working bandwidth is relatively narrower than that in simulation results.

More comprehensive tests are supplemented to thoroughly evaluate the performance of PEFs and the PEFA. Fig. 4a and b illustrate the flapping angles and flapping frequencies of the three PEFs in separate tests. PEFs initially operate in a straight mode and exhibit slight deflection as the wind speed approaches the low critical value. The self-sustained flapping is triggered until the wind speed exceeds the threshold value. For PEF 1 and PEF 2, the flapping angles showcase sustained growth with the wind speed with maximum values of about 100°. Then they suddenly switch to the deflected mode when the wind speed exceeds upper critical values. The flapping frequencies decrease with the wind speed and fall to their lowest points at 5 m/s (PEF 1) and 8 m/s (PEF 2), then slightly rebound and continue to decline until upper critical wind speeds. Different from PEF 1 and 2, PEF 3 is a three-layer

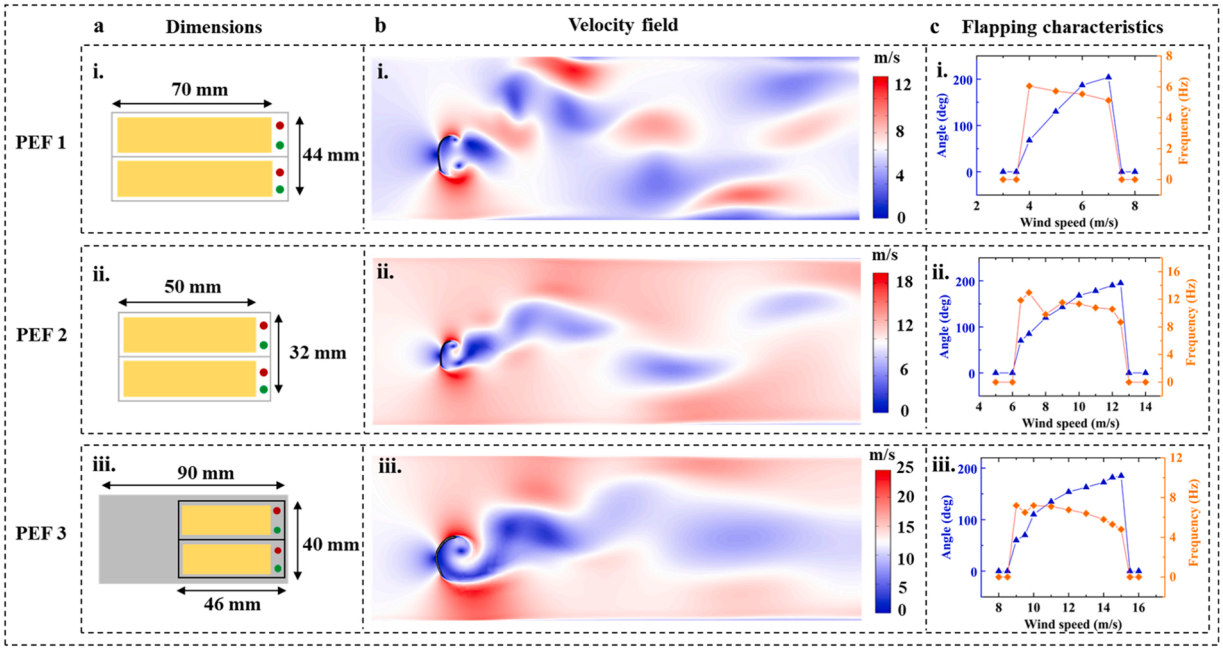

Fig. 3. Design and simulation for PEFs: (a) dimensions of PEFs; (b) screenshots of the simulated fluid velocity field of PEF 1 at 6 m/s, PEF 2 at 10 m/s and PEF 3 at 14 m/s (the simulation time t = 2 T, T is the flapping period of PEFs); (c) simulated flapping characteristics of three PEFs.

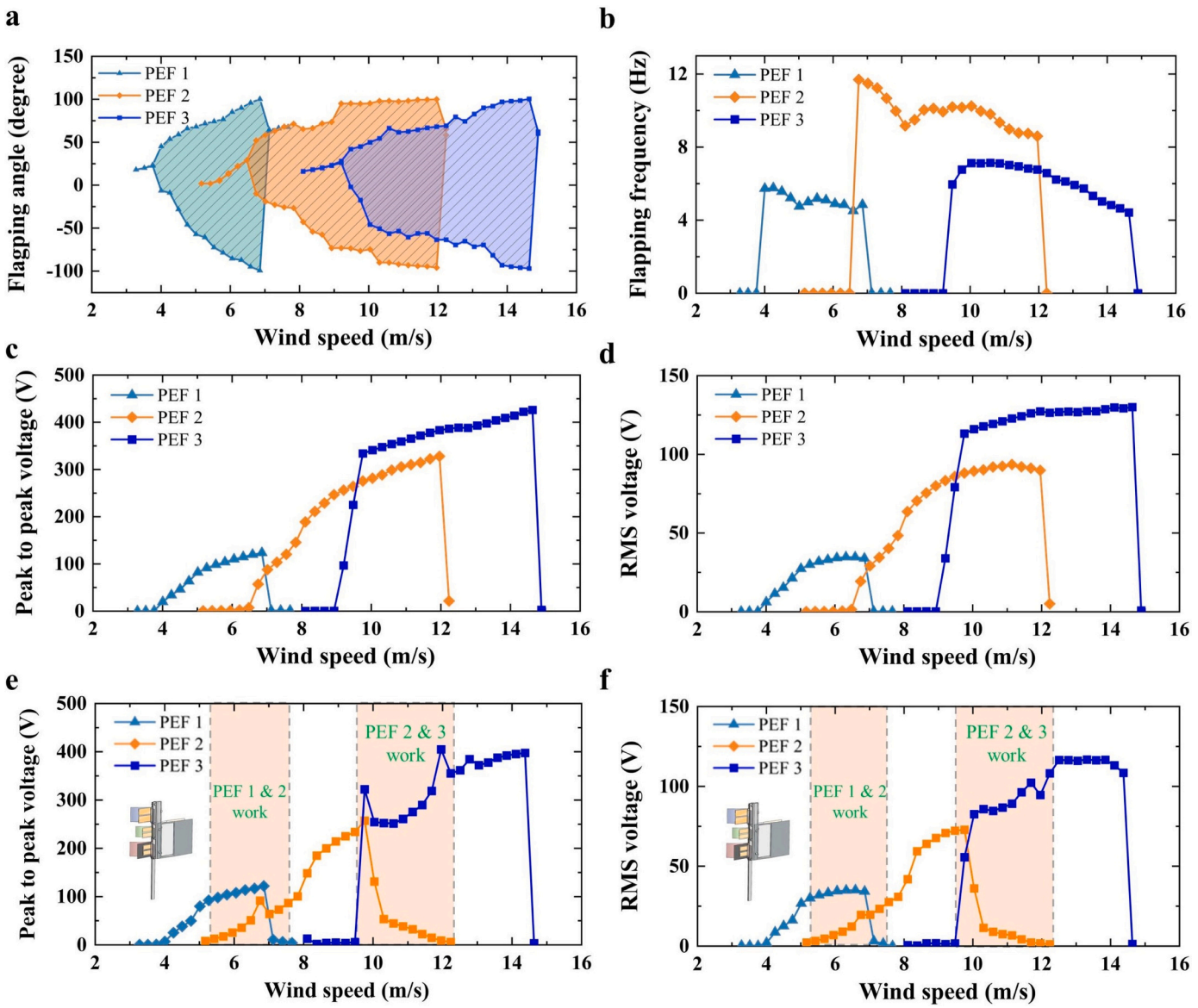

Fig. 4. Performance of PEFs in tests: (a) flapping angle; (b) flapping frequency; (c) peak-to-peak and (d) RMS open-circuit voltage in separate tests; (e) peak-to-peak and (f) RMS open-circuit voltage in tests with three PEFs and the TEF integrated (PVDF films in one PEF are in series connection).

composite structure consisting of two layers of PVDF films and one layer of stainless steel substrate. Its flapping frequency initially rises and then continuously declines with the wind speed in the flapping mode. As depicted in Fig. 4c and d, the generated peak-to-peak voltage during flapping is continuously rising with the wind speed. However, the RMS value slowly increases or slightly decreases as the wind speed approaches the upper critical value, because of the decrease in flapping frequency. The three PEFs achieve maximum peak-to-peak/RMS voltages of 125/34, 328/90, and 426/130 V, and actually cover the wind speed range of 3.7–7, 6.5–12, and 9–14.6 m/s, respectively.

To investigate the aerodynamic effect among flags, the performance of the three PEFs is evaluated when PEFs and the TEF are assembled in an all-in-one structure. As illustrated in Fig. 4e and f, the operational wind speed ranges of PEF 1 and PEF 3 are slightly narrowed, with no significant impact on their voltage performance. The low critical wind speed of PEF 2 is lowered. This is because the flapping of PEF1 induces airflow in the vertical direction, thus triggering PEF 2 to flutter. Meanwhile, the cost is that the upper critical wind speed also decreases. Due to the interference of vertical flapping airflow, two PEFs cannot flap with large amplitudes at the same time. Only when one PEF is in a deflected state, will the other one resume its normal operation. Thus, most performance variations of three PEFs in integrated tests occur when two flags work simultaneously. Overall, the PEFA actually covers a broad operational range of 3.7–14.6 m/s, and the switching between PEFs is smooth. A visual representation of the switching behavior is available in Movie S1.

2.3. Parametric analysis and performance of the TEF

A parametric analysis is conducted to enhance the performance of TEF, and three parameters are considered: the aspect ratio L/W, the longitudinal distance of the clamped leading edge of the flag to baffles D_1, and the lateral distance of baffles to PTFE membrane D_2. The performance of TEF versus aspect ratio (L/W=0.5, 1 and 1.5; W=100 mm) is performed in separate tests while keeping D_1 =L/3 and D_2 =L/10. As shown in Fig. 5a and b, it is evident that the TEF with the aspect ratio of 1.5 demonstrates the best performance and outputs the maximum voltage because of the effective contact area increase. The additional benefit of a larger aspect ratio is the reduction of the low threshold wind speed, indicating the superiority in low-speed wind energy harvesting,

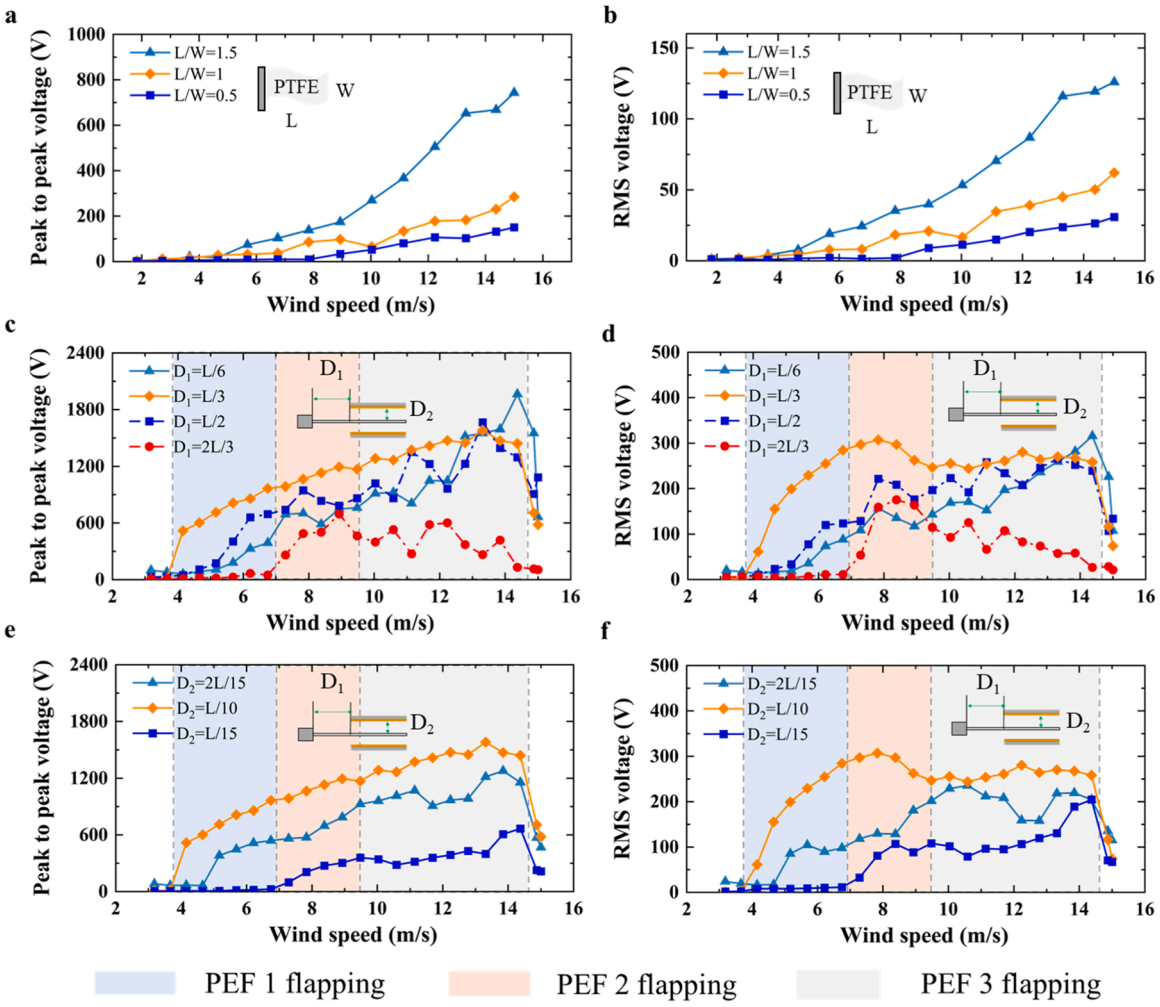

Fig. 5. Parametric analysis and performance of TEF: (a) peak-to-peak and (b) RMS open-circuit voltage with different PTFE lengths (the tests are performed without the combination of PEFA, and D_1=L/3 and D_2 = L/10); (c) peak-to-peak and (d) RMS open-circuit voltage with different distances D_1 (D_2 = L/10); (e) peak-to-peak and (f) RMS open-circuit voltage with different distances D_2 (D_2 = L/3, the optimization of D_1 and D_2 is performed under the combination of PEFA considering its induced complex flow field).

which agrees with the research findings in [67]. Considering the need for a coordinated design and the overall dimensions of FTPNG, the optimal aspect ratio for the TEF is finally determined to be 1.5.

Given the cable housing box behind the flagpole, distances D_1 and D_2 require special attention to ensure the effectiveness flow of wind. In light of the intricate flow field under the PEF flapping, the optimization of D_1 and D_2 is conducted with the integration of the TEF with the PEFA. As illustrated in Fig. 5c and d, the overall performance when D_1 =L/6 is lower than that when D_1 =L/3 despite the largest ideal contact area because a small longitudinal gap restricts sufficient airflow. As D_1 increases to L/2 and 2 L/3, these gaps allow for more airflow but lead to a reduction in the available contact area. Concurrently, the TEF is more likely to get stuck or slide outside the baffles. An optimal balance between the contact area and airflow passage is achieved when D_1 =L/3, thus yielding the highest power generation. As shown in Fig. 5e and f, the lowest threshold speed and maximum output voltage is realized when D_2 =L/10. The power generation capacity when D_2 = 2 L/15 is superior at middle wind speeds (9–12 m/s), but unsatisfactory at higher wind speeds. A larger lateral gap facilitates increased airflow but compromises the contact between the PTFE membrane and electrodes when oscillation amplitude is insufficient. Conversely, when D_2 =L/15, the smaller lateral gap creates more opportunity for contact and separation, but hinders airflow from traversing the cable housing box obstruction to reach the PTFE membrane. It also suppresses the fluttering displacement, increasing the likelihood of simultaneous contact between the PTFE membrane and both electrodes. Hence, the optimal values for D_1 and D_2 are finally determined as L/3 and L/10, respectively.

2.4. Quantification of the performance improvement by flapping wakes

The use of bluff bodies and their wakes represents a common means to enhance the structural vibration in their wake regions. Similarly, another crucial function of PEFA is to act as a distinctive bluff body. Its self-sustained flapping induces wakes behind them and results in a vortex street-like phenomenon. PEF 1 is mainly responsible for low-speed wind. When the wind speed is over the upper critical value of 7 m/s, it will be in a deflected state, thus hindering the airflow from passing by. Hence, the TEF should not be installed behind PET 1. To fully utilize the flapping wakes for boosting the TEF performance, the TEF is vertically clamped behind PEF 2 and PEF 3.

Fig. 6a offers a comparative illustration between the flow fields around the TEF without/with the PEFA. A detailed evolution in flow fields at 9 and 14 m/s is illustrated in Figs. S8 and S9. It is observed that the airflow to TEF is governed by the PEFA and fluctuates periodically when configured with the PEFA. Fig. 6b and c depict the voltage of TEF at 9 m/s in the time domain and frequency domain. Introducing the wakes generated by PEF 2 results in a noticeable boost in the RMS

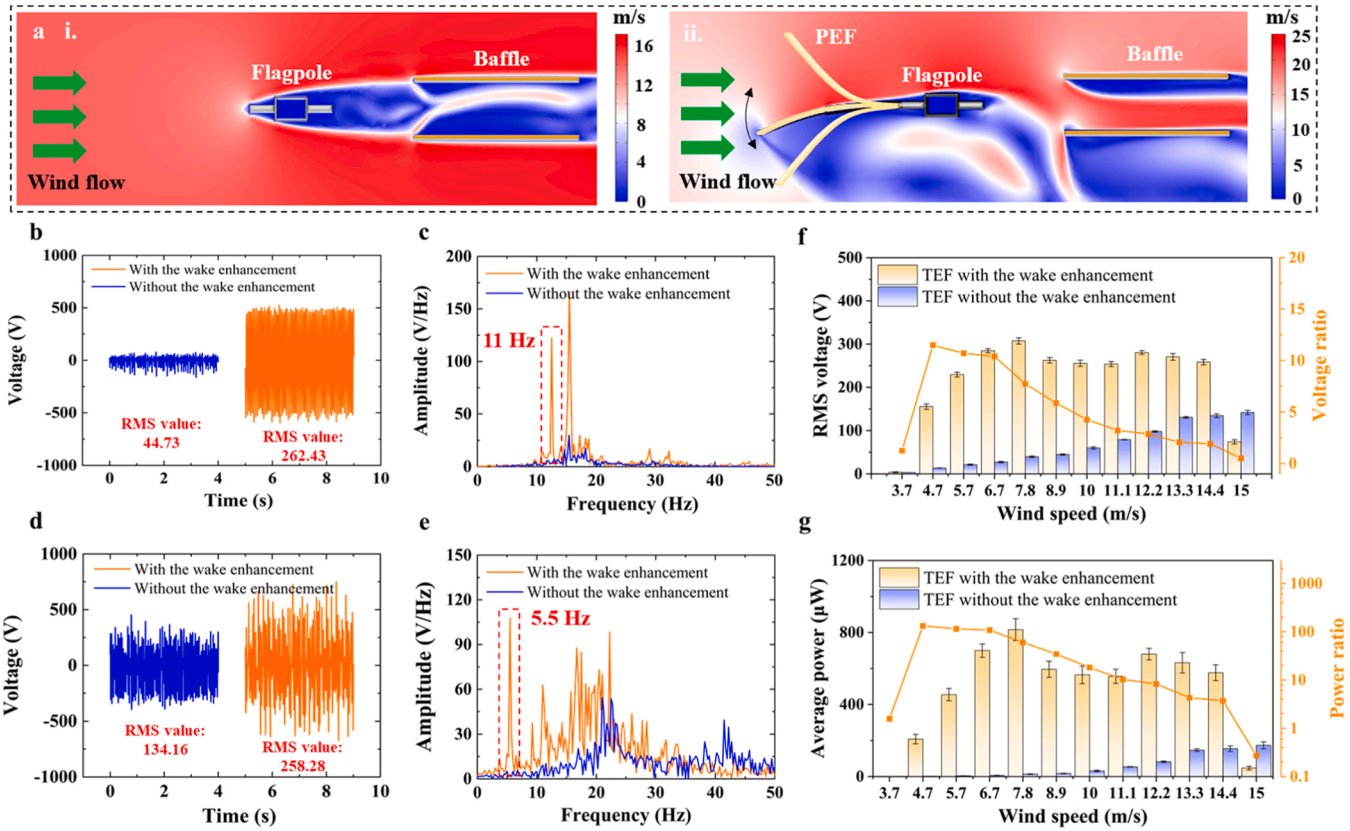

Fig. 6. Performance improvement of TEF contributed by flapping wakes of PEFA (the comparison is performed with the same PTFE length L=150 mm, D_1=L/3, and D_2=L/10): (a) flow field around TEF without/with PEFA; (b) voltage of TEF at 9 m/s in the time domain and (c) the frequency domain; (d) voltage of TEF at 14 m/s in the time domain and (e) the frequency domain; (f) RMS open-circuit voltage and (g) average power improvement with flapping wakes (the external resistance is 50 MΩ).

voltage from 44.73 to 262.43 V. A distinct frequency component at 11 Hz emerges in the frequency domain, corresponding to the flapping frequency of PEF 2. As depicted in Fig. 6d and e, the RMS voltage of TEF at 14 m/s increases from 134.16 to 258.28 V. Similarly, a voltage component with a frequency near the PEF 3 flapping frequency exists in the spectrum and becomes the highest peak, signifying that the fluttering behavior of TEF is now dominated by PEF 3. The benefits of flapping wakes are comprehensively compared in Fig. 6f and g. The boost of RMS voltage can be up to 13 times. Even at the highest power output point of TEF without the wake enhancement at 14.4 m/s, the voltage is doubled. Correspondingly, the average power with an optimal resistance of 50 MΩ can achieve an improvement of nearly 132 times and remain 3.7 times at 14.4 m/s. Note that the RMS voltage and average power slightly decrease at 15 m/s. This is because three PEFs are all deflected, thus hindering the airflow to the TEF to a certain extent.

2.5. Power optimization of the FTPEG

To maximize the harvested energy, the optimal resistances for the three PEFs and the TEF are investigated. As shown in Fig. 7a and b, PEF 1, 2 and 3 yield the maximum average power outputs of 90, 172 and 188 μW with external resistances of 1.5, 4, and 2 MΩ, respectively. When the TEF operates at 9 m/s, an optimal power of 635 μW is delivered with a resistance of 50 MΩ. While, with the wind speed increasing to 14 m/s, the TEF generates a power output of 589 μW with a slightly increased optimal resistance, approximately 60 MΩ. As illustrated in Fig. 7c, peak power outputs of 272, 535, 566 μW can be achieved by the three PEFs, while, a maximum value of 5404 μW can be achieved by the TEF, showcasing its potential for electronics requiring instantaneous high power. Fig. 7d depicts the overall power output incorporating the whole FTPNG. It achieves an operational range from 3.7 to 15 m/s, and a maximum average power of 850 μW at 7.8 m/s. With the boost of PEFA, the TEF accounts for at least 75% of the total output power. The power curve of FTPNG is compared with other FNGs in Fig. S10. The performance of other FNGs steadily rises with the wind speed, while the average power of FTPNG sharply grows with the wind speed until 7.8 m/s, then maintains a high output over 7.8 m/s ≤ U≤ 14.6 m/s (Region B). The FTPNG achieves a 228 μW average output even at 4.7 m/s, which is also a considerably good performance compared with similar nanogenerators. Thereby, the FTPNG ensures reliable high-performance output over a broad range of 4.7–14.6 m/s (Region A).

Furthermore, capacitor charging tests are performed to assess the power generation capacity of the TEF, the PEFA, and the FTPNG, as illustrated in Fig. 7e. When charging a 47 μF capacitor at 9 m/s, the PEFA presents a faster speed, attributed to an order of magnitude smaller internal resistance than that of TEF. With the hybridization of both, the charging speed is further enhanced and the capacitor can be charged to 21 V within 150 s. Fig. 7f compares the charging speed versus different configurations at 6, 9 and 14 m/s. Remarkably, the FTPNG shortens the charging time by 74–76% compared to a single TEF. More charging test results for commonly used capacitors are supplemented in Fig. S11. The hybrid FTPNG encompasses not only the synergy of two energy conversion mechanisms: triboelectrification and piezoelectricity, but also two aerodynamic behaviors of flags: fluttering and flapping. The complementarity between triboelectric and piezoelectric mechanisms enables the harvested electrical energy more easily utilized and stored by conventional electronics. Moreover, electronics with instantaneous high power requirements can also be met by the triboelectric component. The integration of the flapping PEFA and fluttering TEF allows the TEF to achieve higher power performance and an ultra-broad

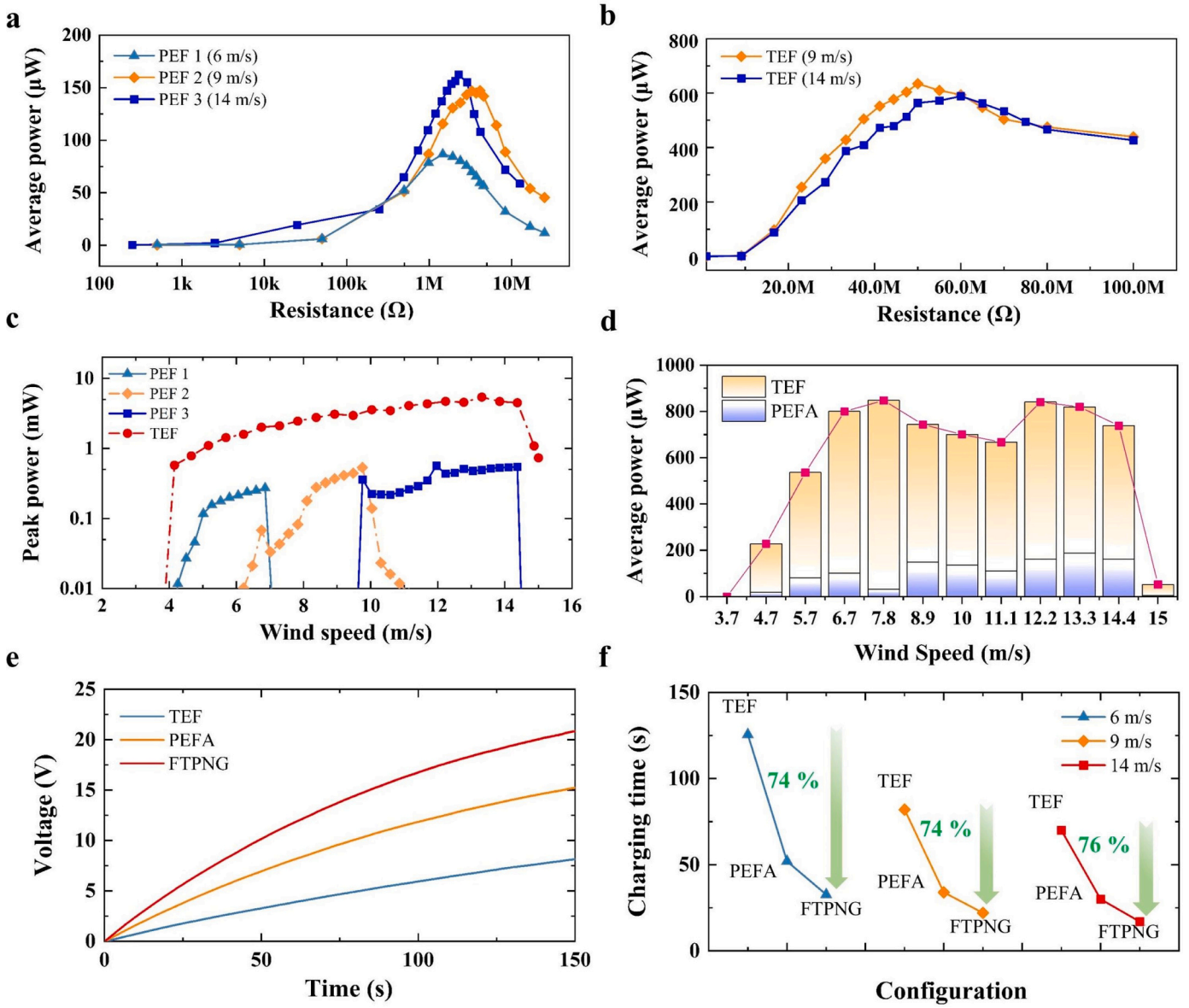

Fig. 7. Power generation optimization of FTPNG: (a) average power of three PEFs versus external resistances; (b) average power of TEF versus external resistances; (c) peak power of three PEFs and TEF with optimized resistances; (d) optimized average power curve of FTPNG; (e) capacitor charging tests for TEF, PEFA and FTPNG with a 47 μF capacitor at 9 m/s; (f) comparison of the time charging a 47 μF capacitor to 5 V at wind speeds of 6 m/s, 9 m/s, and 14 m/s (all the PVDF films in one PEF are in parallel connection during capacitor charging tests).

operational wind speed range. Consequently, the FTPNG can demonstrate better practicality and robustness to adapt to the diverse requirements in various application scenarios.

2.6. Demonstration of powering wireless sensor node

To demonstrate the power generation capacity of FTPNG and its potential as a renewable and sustainable power source, it is employed to power low-power electronics at variable wind speeds. As shown in Fig. 8a, the FTPNG can light 252 LEDs at 9 m/s. 75% of them are powered by TEF, while the rest are powered by PEFA, fully leveraging the high voltage output of TEF. A relevant visual representation of the LED lighting test is provided in Movie S2. Fig. 8b illustrates the application scenario where the WSN with a temperature sensor is powered by the FTPNG. The temperature signal is transmitted to a smartphone via Bluetooth and displayed on the screen of the smartphone. Fig. 8c and d show the photograph and the schematic diagram of the integrated energy harvesting circuit with a WSN incorporating the voltage rectification unit (VRU), the energy management unit (EMU), and the signal transmission unit (STU). In the VRU, all the PVDF films in one PEF are connected in parallel, and then rectified with a bridge rectifier. The rectified voltages of three PEFs and TEF are connected in parallel to charge a filter capacitor. The EMU after the capacitor, employing the chip of LTC-3588–1, is configured to stabilize the voltage and reduce the energy consumption in the circuit. The EMU powers the STU incorporating a CPU, a temperature sensor, and a transceiver for signal acquisition and transmission. The smartphone, as a signal terminal, displays the current temperature situation in real time. As depicted in Fig. 8e, the circuit voltage when powering the WSN will be charged to 5 V first, and then the energy transfer to the STU is triggered with the control of the switch for the temperature signal acquisition and transmission. The PEFA and the TEF demonstrate their independent ability to power the WSN, as well as indicate the potential of FTPNG to simultaneously enable the power supply for multiple sensors. Meanwhile, the whole FTPNG is employed to power the WSN for acquiring signals more frequently. With the wind speed rising from 6 to 14 m/s, the charging

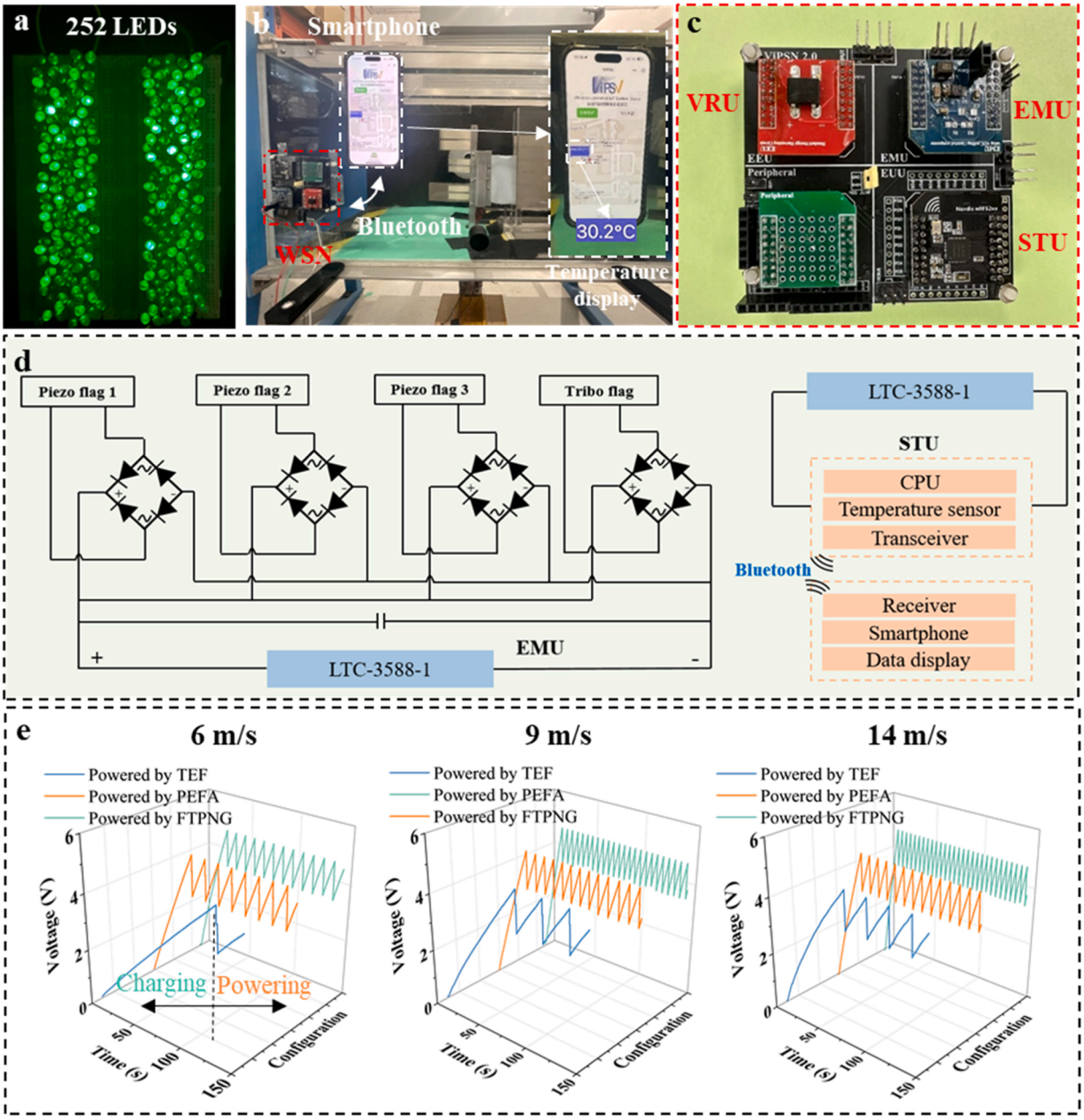

Fig. 8. Demonstration of FTPNG in self-powered systems and WSNs: (a) 252 LEDs in series lighted by FTPNG at 9 m/s; (b) photograph of the WSN powered by FTPNG; (c) detailed view of the integrated energy harvesting circuit with a WSN; (d) schematic diagram of the self-powered WSN; (e) working voltage of the circuit when powering a temperature sensor at wind speeds of 6, 9 and 14 m/s.

time is shortened from 33 to 18 s, as well as the power supply interval from 10 to 5 s. The test results demonstrate a reliable output power of FTPNG over a broad wind speed range, enabling a continuous power supply capacity in scenarios with fluctuating wind speeds. The demonstration video of the self-powered WSN can be found in Movie S3.

3. Conclusion

In summary, we have designed and validated the FTPNG, ensuring a consistent high-performance output exceeding 200 μW over a broad wind speed range of 4.7–14.6 m/s. This robust performance positions the FTPNG as a reliable and continuous power supply solution for WSNs operating in environments characterized by intensely fluctuating wind conditions. To enhance the efficiency of FTPNG, the piezoelectric part is implemented in the form of an array to extend its operational bandwidth and ensure continuous generation of periodic wakes for the TEF. Furthermore, in the optimization process for the TEF, we systematically determine the optimal aspect ratio, longitudinal distance D_1 and lateral distance D_2 to be 1.5, L/3, and L/10, respectively. As a result, the flapping wakes significantly boost the average power of TEF by up to 132 times compared to its performance without wake enhancement. The individual components, PEF 1, PEF 2, PEF 3, and TEF yield maximum average power outputs of 90, 172, 188 and 820 μW at wind speeds of 6.6, 8.9, 13.3 and 7.8 m/s respectively. Collectively, the FTPNG achieves an overall average power of 850 μW at 7.8 m/s. Furthermore, the synergy between triboelectric and piezoelectric mechanisms enables the FTPNG to accelerate the capacitor charging speed by 74–76% compared to a single TEF. In practical demonstration tests, the FTPNG can light 252 LEDs. Both the PEFA and the TEF demonstrate their independent power supply capabilities for the WSN. Even at a relatively low wind speed of 6 m/s, when operating simultaneously, FTPNG guarantees 10-second power supply intervals for the WSN to acquire and transmit

temperature signals, showcasing the potential of FTPNG for applications in the IoTs and various self-powered systems. The proposed FTPNG seamlessly combines flutter-driven and flap-driven nanogenerators and offers valuable guidelines for achieving high-integration and high-performance FNGs.

4. Experimental section

4.1. Fabrication of the FTPNG

The FTPNG mainly comprises the PEFA and the TEF. There are three PEFs in the FTPNG. The PVDF films for PEF 1 are fabricated with an overall geometric dimension of 70 × 0.2 × 22 mm, where the geometric dimension of the PVDF layer is 68 × 0.03 × 19 mm. Two PVDF films in the PEF 1 are connected in parallel with a geometric dimension of 70 × 0.2 × 44 mm. The PVDF films for PEF 2 and 3 are fabricated with an overall geometric dimension of 46 × 0.2 × 16 mm, where the geometric dimension of the PVDF layer is 44 × 0.03 × 12 mm. Two PVDF films in the PEF 2 are connected in parallel with a geometric dimension of 50 × 0.2 × 32 mm. Four PVDF films are attached on both sides of a 304 stainless steel film with a geometric dimension of 90 × 0.1 × 40 mm. The flagpole is made of stainless steel and processed into a rectangle with a geometric dimension of 15 × 4 × 400 mm, and the cable housing box behind the flagpole is made of stainless steel with a geometric dimension of 20 × 10 × 175 mm. The size of the PTFE membrane in the TEF is 150 × 0.1 × 100 mm. The baffles in the TEF are made of Acrylic plates with a thickness of 4 mm, and the contact Area is 100 × 110 mm. Two nickel-coated conductive textiles with a geometric dimension of 100 × 0.05 × 110 mm are attached on the inner side of two baffles.

4.2. Characterization and signal measurement of the FTPNG

The experimental tests for the FTPNG are performed in a wind tunnel with a cross section of 300 (width) × 300 mm (height). The maximum wind speed is 15 m/s. The voltage signal and transfer charge of the FTPNG are measured by an oscilloscope (Tektronix MSO44) and an electrometer (Keithley 6517B). A resistance substitute (IET RS-200 W) and a capacitance substitute (IET RCS-500) are used in the impedance matching tests and capacitor charging tests.

CRediT authorship contribution statement

Liwei Dong: Conceptualization, Writing – original draft, Writing – review & editing, Data curation, Software. **Qian Tang**: Writing – review & editing, Formal analysis. **Chaoyang Zhao:** Methodology, Resources. **Guobiao Hu:** Writing – review & editing, Project administration. **Shuai Qu:** Data curation, Software. **Zicheng Liu:** Data curation, Validation. **Yaowen Yang:** Conceptualization, Writing – review & editing, Funding acquisition, Supervision.

Declaration of Competing Interest

The authors declare that they have no known competing financial interests or personal relationships that could have appeared to influence the work reported in this paper.

Data availability

Data will be made available on request.

Acknowledgments

This work was mainly carried out by the first author during his visit to Nanyang Technological University, and sponsored by the China Scholarship Council (Grant No. 202206260157), and NTU grant 020671-00001.

Appendix A. Supporting information

Supplementary data associated with this article can be found in the online version at doi:10.1016/j.nanoen.2023.109057.

References

[1] I.F. Akyildiz, S. Weilian, Y. Sankarasubramaniam, E. Cayirci, A survey on sensor networks, IEEE Commun. Mag. 40 (2002) 102–114.
[2] S. Sudevalayam, P. Kulkarni, Energy harvesting sensor nodes: survey and implications, IEEE Commun. Surv. Tutor. 13 (2011) 443–461.
[3] J. Zuo, L. Dong, F. Yang, Z. Guo, T. Wang, L. Zuo, Energy harvesting solutions for railway transportation: A comprehensive review, Renewable Energy 202 (2023) 56–87.
[4] F. Yang, J. Li, Y. Long, Z. Zhang, L. Wang, J. Sui, Y. Dong, Y. Wang, R. Taylor, D. Ni, W. Cai, P. Wang, T. Hacker, X. Wang, Wafer-scale heterostructured piezoelectric bio-organic thin films, Science 373 (2021) 337–342.
[5] L. Dong, J. Zuo, T. Wang, W. Xue, P. Wang, J. Li, F Yang, Enhanced piezoelectric harvester for track vibration based on tunable broadband resonant methodology, Energy 254 (2022) 124274.
[6] L. Dong, G. Hu, J. Yu, C. Zhao, S. Qu, Y. Yang, Maximizing onboard power generation of large-scale railway vibration energy harvesters with intricate vehicle-harvester-circuit coupling relationships, Appl. Energy 347 (2023), 121388.
[7] L.C. Rome, L. Flynn, E.M. Goldman, T.D. Yoo, Generating electricity while walking with loads, Science 309 (2005) 1725–1728.
[8] J. Shao, T. Jiang, Z. Wang, Theoretical foundations of triboelectric nanogenerators (TENGs), Sci. China Technol. Sci. 63 (2020) 1087–1109.
[9] G. Hu, C. Zhao, Y. Yang, X. Li, J. Liang, Triboelectric energy harvesting using an origami-inspired structure, Appl. Energy 306 (2022), 118037.
[10] L. He, Y. Han, L. Sun, H. Wang, Z. Zhang, G. Cheng, A rotating piezoelectric-electromagnetic hybrid harvester for water flow energy, Energy Convers. Manag. 290 (2023), 117221.
[11] Ö. Faruk Ünsal, A. Çelik, Bedeloğlu, three-dimensional piezoelectric–triboelectric hybrid nanogenerators for mechanical energy harvesting, ACS Appl. Nano Mater. 6 (2023) 14656–14668.
[12] S. Bai, J. Cui, Y. Zheng, G. Li, T. Liu, Y. Liu, C. Hao, C. Xue, Electromagnetic-triboelectric energy harvester based on vibration-to-rotation conversion for human motion energy exploitation, Appl. Energy 329 (2023), 120292.
[13] K.-J.I. Egbe, A. Matin Nazar, P. Jiao, Piezoelectric-triboelectric-electromagnetic Hybrid Rotational Energy Harvesters (H-REH), Int. J. Mech. Sci. 235 (2022) 107722.
[14] Y.F. Xia, S. Michelin, O. Doare, Resonance-induced enhancement of the energy harvesting performance of piezoelectric flags, Appl. Phys. Lett. 107 (2015).
[15] W. Wang, X. He, X. Wang, M. Wang, K. Xue, A bioinspired structure modification of piezoelectric wind energy harvester based on the prototype of leaf veins, Sens. Actuators A Phys. 279 (2018) 467–473.
[16] S. Lee, S.-H. Bae, L. Lin, Y. Yang, C. Park, S.-W. Kim, S.N. Cha, H. Kim, Y.J. Park, Z. L. Wang, Super-flexible nanogenerator for energy harvesting from gentle wind and as an active deformation sensor, Adv. Funct. Mater. 23 (2013) 2445–2449.
[17] F.-R. Fan, L. Lin, G. Zhu, W. Wu, R. Zhang, Z.L. Wang, Transparent triboelectric nanogenerators and self-powered pressure sensors based on micropatterned plastic films, Nano Letters 12 (2012) 3109–3114.
[18] S. Niu, S. Wang, L. Lin, Y. Liu, Y.S. Zhou, Y. Hu, Z.L. Wang, Theoretical study of contact-mode triboelectric nanogenerators as an effective power source, Energy Environ. Sci. 6 (2013) 3576–3583.
[19] G. Zhu, J. Chen, Y. Liu, P. Bai, Y.S. Zhou, Q. Jing, C. Pan, Z.L. Wang, Linear-grating triboelectric generator based on sliding electrification, Nano Lett. 13 (2013) 2282–2289.
[20] Y. Yang, H. Zhang, J. Chen, Q. Jing, Y.S. Zhou, X. Wen, Z.L. Wang, Single-electrode-based sliding triboelectric nanogenerator for self-powered displacement vector sensor system, ACS Nano 7 (2013) 7342–7351.
[21] M.-H. Yeh, H. Guo, L. Lin, Z. Wen, Z. Li, C. Hu, Z.L. Wang, Rolling friction enhanced free-standing triboelectric nanogenerators and their applications in self-powered electrochemical recovery systems, Adv. Funct. Mater. 26 (2016) 1054–1062.
[22] X. Hui, Z. Li, L. Tang, J. Sun, X. Hou, J. Chen, Y. Peng, Z. Wu, H. Guo, A self-powered highly embedded and sensitive tribo-label-sensor for the fast and stable label printer, Nano-Micro Lett. 15 (2022) 27.
[23] Z. Hu, X. Hui, S. Li, L. Tang, J. Sun, H. Zeng, J. Chen, H. Guo, A self-powered, high-precision and minimum-channel touch panel coupling triboelectrification and uniform resistance film, Nano Energy 114 (2023), 108676.
[24] X. Cao, Y. Xiong, J. Sun, X. Xie, Q. Sun, Z.L. Wang, Multidiscipline applications of triboelectric nanogenerators for the intelligent era of internet of things, Nano-Micro Lett. 15 (2022) 14.
[25] J. Chen, J. Yang, Z. Li, X. Fan, Y. Zi, Q. Jing, H. Guo, Z. Wen, K.C. Pradel, S. Niu, Z. L. Wang, Networks of triboelectric nanogenerators for harvesting water wave energy: a potential approach toward blue energy, ACS Nano 9 (2015) 3324–3331.
[26] A. Ali, H. Shaukat, S. Bibi, W.A. Altabey, M. Noori, S.A. Kouritem, Recent progress in energy harvesting systems for wearable technology, Energy Strategy Rev. 49 (2023), 101124.

[27] Z. Zhao, X. Pu, C. Du, L. Li, C. Jiang, W. Hu, Z.L. Wang, Freestanding flag-type triboelectric nanogenerator for harvesting high-altitude wind energy from arbitrary directions, ACS Nano 10 (2016) 1780–1787.
[28] Y. Wang, E. Yang, T. Chen, J. Wang, Z. Hu, J. Mi, X. Pan, M. Xu, A novel humidity resisting and wind direction adapting flag-type triboelectric nanogenerator for wind energy harvesting and speed sensing, Nano Energy 78 (2020), 105279.
[29] Y. Wang, X. Liu, T. Chen, H. Wang, C. Zhu, H. Yu, L. Song, X. Pan, J. Mi, C. Lee, M. Xu, An underwater flag-like triboelectric nanogenerator for harvesting ocean current energy under extremely low velocity condition, Nano Energy 90 (2021), 106503.
[30] J. Bae, J. Lee, S. Kim, J. Ha, B.-S. Lee, Y. Park, C. Choong, J.-B. Kim, Z.L. Wang, H.-Y. Kim, J.-J. Park, U.I. Chung, Flutter-driven triboelectrification for harvesting wind energy, Nat. Commun. 5 (2014) 4929.
[31] J.-h Son, S.-H. Chung, K. Cha, S. Kim, Z.-H. Lin, J. Hong, J. Chung, S. Lee, Ultrahigh performance, serially stackable, breeze driven triboelectric generator via ambient air ionizing channel, Adv. Mater. 35 (2023) 2300283.
[32] W. Sun, Z. Ding, Z. Qin, F. Chu, Q. Han, Wind energy harvesting based on fluttering double-flag type triboelectric nanogenerators, Nano Energy 70 (2020), 104526.
[33] H. Liu, H. Fu, L. Sun, C. Lee, E.M. Yeatman, Hybrid energy harvesting technology: from materials, structural design, system integration to applications, Renew. Sustain. Energy Rev. 137 (2021), 110473.
[34] Y. Yan, J. Zhu, Y. Zhang, Z. Wang, L. Jiang, Z.L. Wang, J. Zhu, T. Cheng, Triboelectric-electromagnetic hybrid generator with swing-blade structures for effectively harvesting distributed wind energy in urban environments, Nano Res. (2023).
[35] K. Fan, C. Chen, B. Zhang, X. Li, Z. Wang, T. Cheng, Z. Lin Wang, Robust triboelectric-electromagnetic hybrid nanogenerator with maglev-enabled automatic mode transition for exploiting breeze energy, Appl. Energy 328 (2022), 120218.
[36] H. Dang, Y. Wang, S. Zhang, Q. Gao, X. Li, L. Wan, Z.L. Wang, T. Cheng, Triboelectric-electromagnetic hybrid generator with the inertia-driven conversion mechanism for wind energy harvesting and scale warning, Mater. Today Energy 29 (2022), 101136.
[37] C. Zhang, W. Tang, C. Han, F. Fan, Z.L. Wang, Theoretical comparison, equivalent transformation, and conjunction operations of electromagnetic induction generator and triboelectric nanogenerator for harvesting mechanical energy, Adv. Mater. 26 (2014) 3580–3591.
[38] Y. Zi, H. Guo, Z. Wen, M.-H. Yeh, C. Hu, Z.L. Wang, Harvesting low-frequency (<5 Hz) irregular mechanical energy: a possible killer application of triboelectric nanogenerator, ACS Nano 10 (2016) 4797–4805.
[39] Q. Wang, H.-X. Zou, L.-C. Zhao, M. Li, K.-X. Wei, L.-P. Huang, W.-M. Zhang, A synergetic hybrid mechanism of piezoelectric and triboelectric for galloping wind energy harvesting, Appl. Phys. Lett. 117 (2020).
[40] Q. Wang, Z. Chen, L. Zhao, M. Li, H. Zou, K. Wei, X. Zhang, W. Zhang, Enhanced galloping energy harvester with cooperative mode of vibration and collision, Appl. Math. Mech. 43 (2022) 945–958.
[41] H.-X. Zou, L.-C. Zhao, Q. Wang, Q.-H. Gao, G. Yan, K.-X. Wei, W.-M. Zhang, A self-regulation strategy for triboelectric nanogenerator and self-powered wind-speed sensor, Nano Energy 95 (2022), 106990.
[42] C. Ye, K. Dong, J. An, J. Yi, X. Peng, C. Ning, Z.L. Wang, A triboelectric–electromagnetic hybrid nanogenerator with broadband working range for wind energy harvesting and a self-powered wind speed sensor, ACS Energy Lett. 6 (2021) 1443–1452.
[43] J. Silva-Leon, A. Cioncolini, M.R.A. Nabawy, A. Revell, A. Kennaugh, Simultaneous wind and solar energy harvesting with inverted flags, Appl. Energy 239 (2019) 846–858.
[44] L.-C. Zhao, H.-X. Zou, K.-X. Wei, S.-X. Zhou, G. Meng, W.-M. Zhang, Mechanical intelligent energy harvesting: from methodology to applications, Adv. Energy Mater. 13 (2023) 2300557.
[45] H.-X. Zou, L.-C. Zhao, Q.-H. Gao, L. Zuo, F.-R. Liu, T. Tan, K.-X. Wei, W.-M. Zhang, Mechanical modulations for enhancing energy harvesting: principles, methods and applications, Appl. Energy 255 (2019), 113871.
[46] S. Orrego, K. Shoele, A. Ruas, K. Doran, B. Caggiano, R. Mittal, S.H. Kang, Harvesting ambient wind energy with an inverted piezoelectric flag, Appl. Energy 194 (2017) 212–222.
[47] M. Tang, Q. Guan, X. Wu, X. Zeng, Z. Zhang, Y. Yuan, A high-efficiency multidirectional wind energy harvester based on impact effect for self-powered wireless sensors in the grid, Smart Mater. Struct. 28 (2019), 115022.
[48] M. Xu, Y.-C. Wang, S.L. Zhang, W. Ding, J. Cheng, X. He, P. Zhang, Z. Wang, X. Pan, Z.L. Wang, An aeroelastic flutter based triboelectric nanogenerator as a self-powered active wind speed sensor in harsh environment, Extrem. Mech. Lett. 15 (2017) 122–129.
[49] Y. Xia, Y. Tian, L. Zhang, Z. Ma, H. Dai, B. Meng, Z. Peng, An optimized flutter-driven triboelectric nanogenerator with a low cut-in wind speed, Micromachines 12 (2021) 366.
[50] B.S.H. Connell, D.K.P. Yue, Flapping dynamics of a flag in a uniform stream, J. Fluid Mech. 581 (2007) 33–67.
[51] S. Alben, M.J. Shelley, Flapping states of a flag in an inviscid fluid: bistability and the transition to chaos, Phys. Rev. Lett. 100 (2008), 074301.
[52] S. Chawdhury, G. Morgenthal, A partitioned solver to simulate large-displacement fluid–structure interaction of thin plate systems for vibration energy harvesting, Comput. Struct. 224 (2019), 106110.
[53] G.W. Taylor, J.R. Burns, S.A. Kammann, W.B. Powers, T.R. Welsh, The energy harvesting eel: a small subsurface ocean/river power generator, IEEE J. Ocean. Eng. 26 (2001) 539–547.
[54] J.J. Allen, A.J. Smits, Energy harvesting eel, J. Fluids Struct. 15 (2001) 629–640.
[55] Y. Hu, B. Yang, X. Chen, X. Wang, J. Liu, Modeling and experimental study of a piezoelectric energy harvester from vortex shedding-induced vibration, Energy Convers. Manag. 162 (2018) 145–158.
[56] J. Wang, S. Sun, G. Hu, Y. Yang, L. Tang, P. Li, G. Zhang, Exploring the potential benefits of using metasurface for galloping energy harvesting, Energy Convers. Manag. 243 (2021), 114414.
[57] J. Wang, Y. Zhang, M. Liu, G. Hu, Etching metasurfaces on bluff bodies for vortex-induced vibration energy harvesting, Int. J. Mech. Sci. 242 (2023), 108016.
[58] J. Wang, S. Sun, L. Tang, G. Hu, J. Liang, On the use of metasurface for Vortex-Induced vibration suppression or energy harvesting, Energy Convers. Manag. 235 (2021), 113991.
[59] U. Latif, E.H. Dowell, E. Uddin, M. Yamin, Younis, Parametric aerodynamic and aeroelastic study of a deformable flag-based energy harvester for powering low energy devices, Energy Convers. Manag. 280 (2023), 116846.
[60] U. Latif, M.Y. Younis, E. Uddin, Z. Ali, A. Mubashar, A. Abdelkefi, Impact of solid and hollow bluff bodies on the performance and dynamics of flag-based energy harvester, Sustain. Energy Technol. Assess. 55 (2023), 102882.
[61] U. Latif, M.Y. Younis, S. Idrees, E. Uddin, A. Abdelkefi, A. Munir, M. Zhao, Synergistic analysis of wake effect of two cylinders on energy harvesting characteristics of piezoelectric flag, Renew. Sustain. Energy Rev. 173 (2023), 113114.
[62] Y. Zhang, S.-C. Fu, K.C. Chan, D.-M. Shin, C.Y.H. Chao, Boosting power output of flutter-driven triboelectric nanogenerator by flexible flagpole, Nano Energy 88 (2021), 106284.
[63] P. Li, D. Zhang, W. Peng, J. Cui, Y. Yang, Static aeroelastic instability analysis of an inverted plate in ground effect and comparison with a wind-tunnel test, J. Fluids Struct. 116 (2023), 103790.
[64] D. Kim, J. Cossé, C. Huertas Cerdeira, M. Gharib, Flapping dynamics of an inverted flag, J. Fluid Mech. 736 (2013) R1.
[65] J. Ryu, S.G. Park, B. Kim, H.J. Sung, Flapping dynamics of an inverted flag in a uniform flow, J. Fluids Struct. 57 (2015) 159–169.
[66] K. Shoele, R. Mittal, Energy harvesting by flow-induced flutter in a simple model of an inverted piezoelectric flag, J. Fluid Mech. 790 (2016) 582–606.
[67] C. Eloy, R. Lagrange, C. Souilliez, L. Schouveiler, Aeroelastic instability of cantilevered flexible plates in uniform flow, J. Fluid Mech. 611 (2008) 97–106.

Liwei Dong is a PhD candidate in the Institute of Rail Transitat Tongji University, and a visiting student in the School of Civil and Environmental Engineering at Nanyang Technological University. His research interests include wind and mechanical energy harvesting, intelligent sensing and interface circuits for energy harvesting.

Qian Tang received his Ph.D. degree in Applied Physics from Chongqing University, China. Now he is working in the Chongqing Key Laboratory of Green Energy Materials Technology and System, Chongqing University of Technology, Chongqing, China. His current research interest is triboelectric nanogenerator based self-poweredsystems.

Chaoyang Zhao obtained his Ph.D. from Nanyang Technological University (NTU) in 2023. He joined Professor Yang Yaowen's research group in 2018 and currently working as a Research Fellow at NTU. His research interests mainly focus on energy harvesting, nonlinear dynamics, structural health monitoring and composite sensors.

Guobiao Hu received his B.Eng. degree from Southwest Jiaotong University, China, in 2012, Diplôme d'Ingénieur from École Centrale Paris, France, in 2015, and Ph.D. degree from the University of Auckland, New Zealand, in 2020. He is currently a tenure-track Assistant Professor with the Internet of Things Thrust, Information Hub, the Hong Kong University of Science and Technology (Guangzhou), China. His research interests include vibration & wind energy harvesting and acoustic-elastic metamaterials.

Shuai Qu received his bachelor's degree from Southwest Jiaotong University, Chengdu, China, in 2018 and is currently pursuing his Ph.D. there. Bridging the realms of rail transit dynamics, his research delves into intelligent sensing of structural service conditions, metamaterial-based vibration control, and deep learning-driven dynamics elucidation.

Zicheng Liuis a PhD candidate in the School of Civil and Environmental Engineering at Nanyang Technological University. His research interest is in vibration energy harvesting using triboelectric materials.

Yaowen Yang is currently a Professor in the School of Civil and Environmental Engineering, Nanyang Technological University, Singapore. He is an expert researcher in the areas of small energy harvesting and structural and geotechnical monitoring. His research encompasses aeroelastic and vibration energy harvesting, metamaterials, structural health monitoring, and uncertainty analysis in structural dynamics. Prof. Yang has secured substantial research grants from various funding sources and industry partners, resulting in over 280 publications in journals and conferences. Prof Yang received his B.Eng and M.Eng from Shanghai Jiao Tong University and Ph.D from Nanyang Technological University.